
Traction Dynamics of Filopodia on Compliant Substrates

Author(s): Clarence E. Chan and David J. Odde

Source: *Science*, New Series, Vol. 322, No. 5908 (Dec. 12, 2008), pp. 1687-1691

Published by: American Association for the Advancement of Science

Stable URL: <https://www.jstor.org/stable/20177015>

Accessed: 25-01-2020 17:43 UTC

REFERENCES

Linked references are available on JSTOR for this article:

https://www.jstor.org/stable/20177015?seq=1&cid=pdf-reference#references_tab_contents

You may need to log in to JSTOR to access the linked references.

JSTOR is a not-for-profit service that helps scholars, researchers, and students discover, use, and build upon a wide range of content in a trusted digital archive. We use information technology and tools to increase productivity and facilitate new forms of scholarship. For more information about JSTOR, please contact support@jstor.org.

Your use of the JSTOR archive indicates your acceptance of the Terms & Conditions of Use, available at <https://about.jstor.org/terms>



American Association for the Advancement of Science is collaborating with JSTOR to digitize, preserve and extend access to *Science*

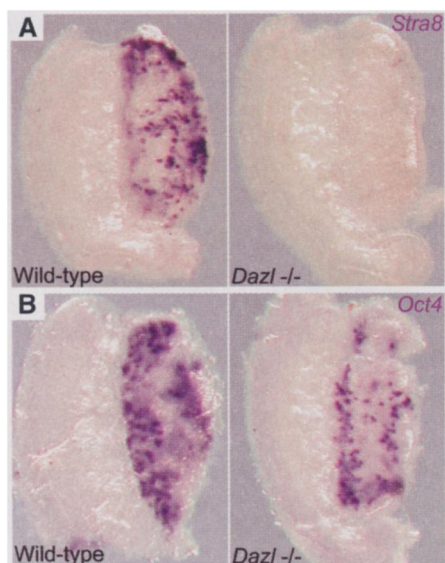


Fig. 3. *Dazl* is required for RA-induced expression of *Stra8* in embryonic testes. Whole-mount in situ hybridization for (A) *Stra8* mRNA and (B) *Oct4* mRNA in wild-type and *Dazl*-deficient testes dissected at E12.5 and cultured for 48 hours in the presence of 0.7 μ M RA is shown.

1, E and F). Similarly, *Rec8* exhibited little or no expression in *Dazl*-deficient ovaries (Fig. 1F). Thus, *Dazl* is required for both *Stra8*-mediated initiation of meiosis in female germ cells and *Stra8*-independent expression of *Sycp3* and *Rec8* there.

We propose a pathway by which embryonic germ cells advance from a primordial state to the initiation of meiosis (Fig. 2). This pathway includes a newly posited cell state, the meiosis-competent gonocyte, whose derivation from a primordial germ cell requires the germ cell-intrinsic factor *Dazl* and whose progression to meiotic initiation and prophase in the female germ line requires the extrinsic meiosis-inducing factor RA and *Stra8*. We propose that this meiosis-competent cell state exists in both male and female embryonic germ lines, despite the fact that meiosis does not initiate in male embryos. The posited meiosis-competent gonocyte contains SYCP3 protein not yet loaded onto chromosomes (Fig. 2), which is consistent with the observation (6) that both male and female embryonic germ cells express SYCP3 protein before the sexes take different paths: Female germ cells advance to meiotic prophase, where SYCP3 functions, whereas male germ cells down-regulate SYCP3 and arrest in G_0 .

Embryonic testicular germ cells express *Stra8* when exposed to exogenous RA, even though they normally express *Stra8* only after birth (9, 10). Our model predicts that ectopic expression of *Stra8* in RA-treated embryonic testes should require *Dazl* function. We dissected testes from wild-type and *Dazl*-deficient E12.5 embryos, cultured them in the presence of 0.7 μ M RA for 48 hours, and assayed *Stra8* expression by whole-mount in situ hybridization. As previously reported (9, 10), RA induced robust expression of *Stra8* in wild-type testes (Fig.

3A). In contrast, in *Dazl*-deficient testes, no induction was observed (Fig. 3A). To confirm that this failure to induce *Stra8* expression in *Dazl*-deficient testes was not due to germ cell apoptosis (19), we performed a control in situ hybridization for *Oct4* (Mouse Genome Informatics ID *Pou5f1*), a gene expressed in embryonic germ cells but not in gonadal somatic cells (26). We observed abundant *Oct4* expression in RA-cultured testes, both wild-type and *Dazl*-deficient (Fig. 3B). Thus, expression of *Stra8* in response to RA requires *Dazl* in embryonic testes and ovary alike, confirming that *Dazl* is a competence factor for meiotic initiation in embryos of both sexes.

In *S. cerevisiae* cells, expression of the a/a mating-type heterodimer is a prerequisite to launching the meiotic initiation program in response to an extrinsic cue. Our findings demonstrate that *Dazl* plays an analogous role in embryonic mice. In both a unicellular eukaryote and a complex animal, meiotic initiation is governed by a cell-intrinsic competence factor and an extrinsic inducing signal.

References and Notes

1. A. G. Byskov, *Nature* **252**, 396 (1974).
2. A. G. Byskov, L. Saxen, *Dev. Biol.* **52**, 193 (1976).
3. S. Upadhyay, L. Zamboni, *Proc. Natl. Acad. Sci. U.S.A.* **79**, 6584 (1982).
4. A. McLaren, *J. Exp. Zool.* **228**, 167 (1983).
5. A. McLaren, D. Southey, *Dev. Biol.* **187**, 107 (1997).
6. A. D. Di Carlo, G. Travia, M. De Felici, *Int. J. Dev. Biol.* **44**, 241 (2000).
7. D. B. Menke, J. Koubova, D. C. Page, *Dev. Biol.* **262**, 303 (2003).
8. A. E. Baltus et al., *Nat. Genet.* **38**, 1430 (2006).
9. J. Bowles et al., *Science* **312**, 596 (2006).
10. J. Koubova et al., *Proc. Natl. Acad. Sci. U.S.A.* **103**, 2474 (2006).
11. M. Mark, N. B. Ghyselinck, P. Chambon, *Annu. Rev. Pharmacol. Toxicol.* **46**, 451 (2006).
12. S. M. Honigberg, K. Purnapatre, *J. Cell Sci.* **116**, 2137 (2003).
13. A. K. Hopper, B. D. Hall, *Genetics* **80**, 41 (1975).
14. J. Seligman, D. C. Page, *Biochem. Biophys. Res. Commun.* **245**, 878 (1998).
15. H. J. Cooke, M. Lee, S. Kerr, M. Ruggiu, *Hum. Mol. Genet.* **5**, 513 (1996).
16. M. Ruggiu et al., *Nature* **389**, 73 (1997).
17. B. H. Schrans-Stassen, P. T. Saunders, H. J. Cooke, D. G. de Rooij, *Biol. Reprod.* **65**, 771 (2001).
18. P. T. Saunders et al., *Reproduction* **126**, 589 (2003).
19. Y. Lin, D. C. Page, *Dev. Biol.* **288**, 309 (2005).
20. Materials and methods are available as supporting material on Science Online.
21. M. Ginsburg, M. H. Snow, A. McLaren, *Development* **110**, 521 (1990).
22. Y. Toyooka et al., *Mech. Dev.* **93**, 139 (2000).
23. E. P. Rogakou, D. R. Pilch, A. H. Orr, V. S. Ivanova, W. M. Bonner, *J. Biol. Chem.* **273**, 5858 (1998).
24. L. A. Bannister, J. C. Schimenti, *Cytogenet. Genome Res.* **107**, 191 (2004).
25. H. Scherthan, *Cytogenet. Genome Res.* **103**, 235 (2003).
26. M. Pesce, X. Wang, D. J. Wolgemuth, H. Scholer, *Mech. Dev.* **71**, 89 (1998).
27. We thank H. Cooke for mice carrying the *Dazl*^{tm1Hgu} allele; C. Heyting for SYCP3 antisera; T. Noce for MVH antisera; and A. Amon, E. Anderson, A. Baltus, A. Bortvin, M. Carmell, G. Fink, A. Hochwagen, Y. Hu, J. Lange, J. Mueller, L. Okumura, and T. Orr-Weaver for advice and comments on the manuscript. Microscopy and image capture were conducted at the W. M. Keck Foundation Biological Imaging Facility at the Whitehead Institute. This work was supported by the Howard Hughes Medical Institute.

Supporting Online Material

www.sciencemag.org/cgi/content/full/322/5908/1685/DC1

Materials and Methods

Fig. S1

References

24 September 2008; accepted 30 October 2008

10.1126/science.1166340

Traction Dynamics of Filopodia on Compliant Substrates

Clarence E. Chan and David J. Odde*

Cells sense the environment's mechanical stiffness to control their own shape, migration, and fate. To better understand stiffness sensing, we constructed a stochastic model of the "motor-clutch" force transmission system, where molecular clutches link F-actin to the substrate and mechanically resist myosin-driven F-actin retrograde flow. The model predicts two distinct regimes: (i) "frictional slippage," with fast retrograde flow and low traction forces on stiff substrates and (ii) oscillatory "load-and-fail" dynamics, with slower retrograde flow and higher traction forces on soft substrates. We experimentally confirmed these model predictions in embryonic chick forebrain neurons by measuring the nanoscale dynamics of single-growth-cone filopodia. Furthermore, we experimentally observed a model-predicted switch in F-actin dynamics around an elastic modulus of 1 kilopascal. Thus, a motor-clutch system inherently senses and responds to the mechanical stiffness of the local environment.

Recent work has demonstrated the importance of substrate stiffness on cell motility, morphology, and fate (1). For instance, fibroblasts display a behavior known as durotaxis, preferentially migrating toward regions of higher stiffness (2). Softer substrates have been shown to promote branching in primary mouse spinal cord neurons while suppress-

ing the growth of associated glia (3, 4). A recent study has also shown that mesenchymal stem cell fate can be determined by the stiffness of the

Department of Biomedical Engineering, University of Minnesota, Minneapolis, MN 55455, USA.

*To whom correspondence should be addressed. E-mail: oddex002@umn.edu

culture substrate, a phenomenon that requires actomyosin contractility (5). Although the importance of actomyosin and substrate adhesions are well appreciated, it is not clear how these components work together to sense and respond to the stiffness of the local environment.

One way cells are thought to probe their environment is through the generation of traction by a “motor-clutch” mechanism where cells utilize molecular clutches to physically link F-actin to the extracellular substrate (6). By creating this physical coupling, cells are thought to create a frictional slippage interface that transmits traction forces and slows F-actin retrograde flow, allowing actin polymerization to advance the leading edge (7–9). If cells use the motor-clutch system to probe their mechanical environment, we

wondered how this system would be influenced by substrate stiffness.

To address this question, we first constructed a stochastic physical model of the motor-clutch hypothesis, treating molecular clutches and the substrate as simple, Hookean springs (Fig. 1A). At every time step, n_m myosin motors drive retrograde flow by exerting a force F_M on an F-actin bundle. Next, individual molecular clutches are allowed to reversibly engage the F-actin bundle with rate constants k_{on} and k_{off} . Clutches that successfully engage will build tension with spring constant κ_c , as they are stretched by retrograde motion of F-actin. Tension along engaged clutches increases their off-rate constant, k_{off}^* , exponentially according to Bell's Law (10), with a characteristic breaking

force F_b . Tension in the engaged molecular clutches sums to a traction force that must be balanced by tension and deformation in the compliant substrate with spring constant κ_{sub} . Myosin motors work against this load force, slowing their motor sliding velocity according to a linear force-velocity relation. Finally, actin polymerizes at the plus end of the F-actin bundle with constant velocity to counter retrograde flow and maintain the F-actin bundle. For simplicity, we ignored tension-dependent strengthening of adhesions, as has been reported in some cases (11, 12), as this effect can be added later to increase the model sophistication and complexity if necessary (13).

When we simulated the motor-clutch system on compliant substrates, we observed the emergence of two distinct traction force dynamics

Fig. 1. A model for motor-clutch motility on compliant substrates predicts substrate stiffness-dependent dynamics. **(A)** Schematic representation of a mechano-chemical motor-clutch model. Myosin motors pull an F-actin filament bundle to the left with force, F_M , at velocity, v_{filament} . Molecular clutches reversibly engage the F-actin bundle with rates k_{on} and k_{off} to resist retrograde flow. During loading, the clutches are stretched to strains $x_{\text{clutch}(i)}$, and they tend to fail with a force-dependent off rate, k_{off}^* . Transmitted forces induce a local substrate strain, x_{sub} . The mechanical stiffness of the clutches, κ_c , and of the substrate, κ_{sub} , determine the mechanical resistance to loading. **(B)** Model-predicted substrate stiffness-dependent clutch dynamics. Red markers indicate the initial position of the bundle and substrate and highlight their relative motion. Green markers indicate the initial F-actin bundle position. Stiff substrates exhibit frictional slippage, in which the F-actin bundle constantly slides relative to the substrate (red markers move apart). Soft substrates exhibit load-and-fail dynamics, where the compliant substrate moves with the F-actin bundle until coupling failure. **(C)** Model-predicted substrate position as a function of time highlights load-and-fail on compliant substrates (blue line). Stiff substrates exhibit frictional slippage (red line, also see inset). **(D)** Load-and-fail clutch dynamics are predicted to lead to slower time-averaged F-actin retrograde flow rates and higher traction forces, whereas frictional slippage dynamics lead to increased retrograde flow rates and decreased traction force. The transition zone (light blue area) defines a region of greatest sensitivity to substrate stiffness.

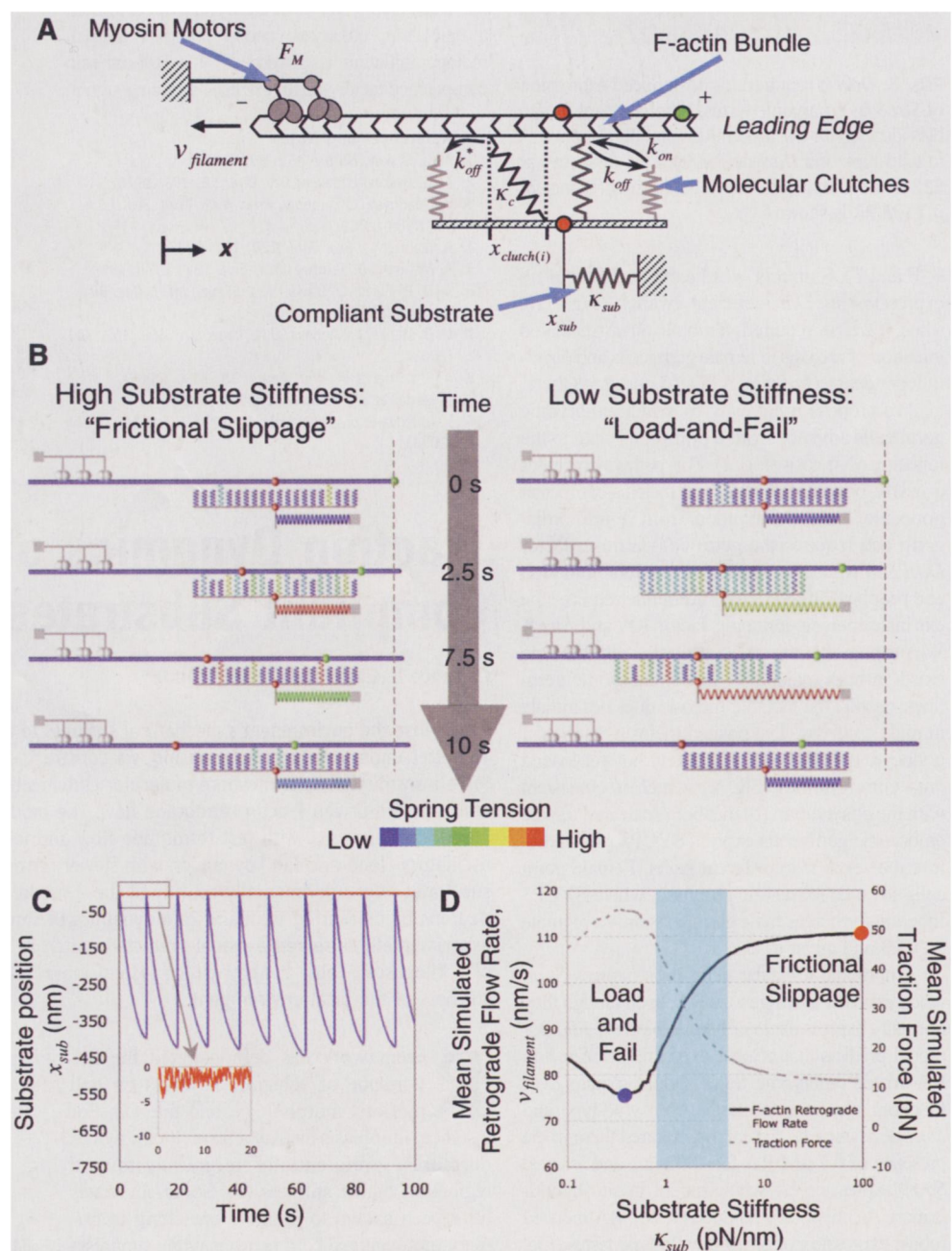


(Fig. 1B and movie S1). On stiff substrates, molecular clutches engage the F-actin bundle but abruptly disengage as lack of compliance in the substrate results in a rapid building of tension within engaged clutches that drastically shortens F-actin/clutch interaction lifetimes. In this case, the F-actin bundle is continuously slipping from the point of contact at a roughly constant velocity. We describe this dynamic as “frictional slip-

page,” a behavior that has previously been observed on stiff glass substrates (7, 14, 15).

On soft substrates, substrate compliance slows the rate at which tension builds along individually engaged clutches. This prolongs F-actin/clutch interaction times, with most clutches remaining engaged to the F-actin bundle at early times in the cycle (Fig. 1B and movie S1). During this time, there is little relative mo-

tion between the F-actin bundle and the substrate as tension slowly develops within the substrate. Because of this lack of resistance, myosin motors work near their unloaded sliding velocity, leading to high rates of F-actin retrograde flow and a slight retraction of the leading edge. As the substrate strains and greater tension builds, clutches largely remain engaged due to sharing of the mechanical load among engaged neighbors. This

Fig. 2. Growth-cone filopodia on compliant substrates exert traction forces with load-and-fail dynamics. (A) Montage of a GFP-actin transfected ECFN growth cone on a 730-Pa PAG with embedded fiducial marker beads acquired at 3-s intervals. A reporter bead underneath a growth-cone filopodium displays periodic motions. Blue arrowheads indicate initial position; yellow arrowheads indicate position at the given time point. The rectangular box indicates a traction-producing filopodium. (B) Time projection of the image stack over 5 min. The marker bead in (A) appears as a line (blue and yellow arrowheads). The reference bead (white arrowhead) appears as a single spot. A second marker bead (gray arrowheads) was also pulled retrogradely, as evidenced by the elongated appearance. (C) Kymograph of the region indicated in (A). Yellow arrowheads indicate abrupt failure events. (D) Marker bead position recorded at 100-ms intervals.

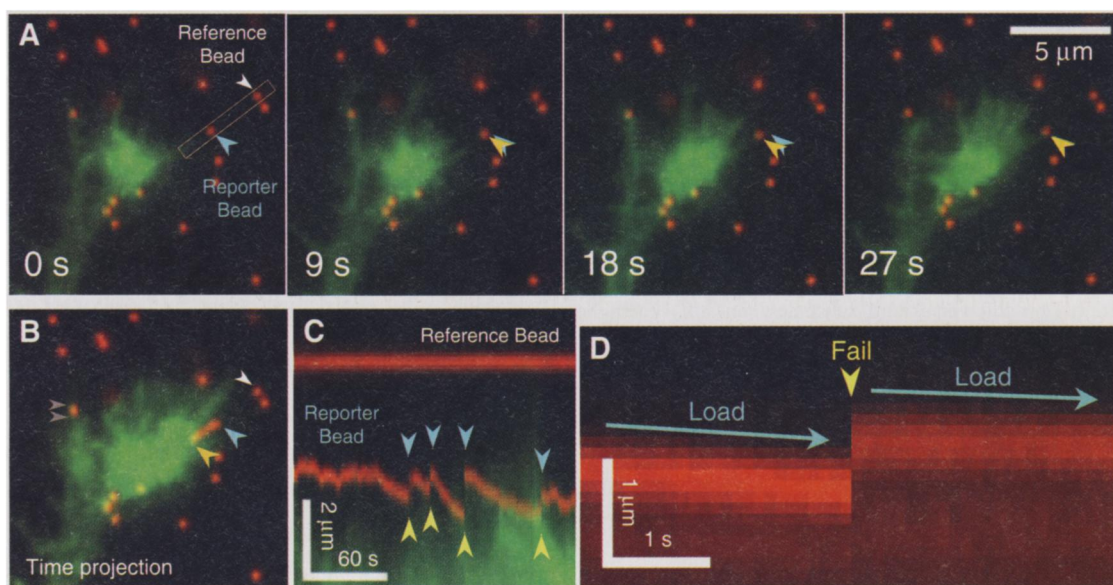
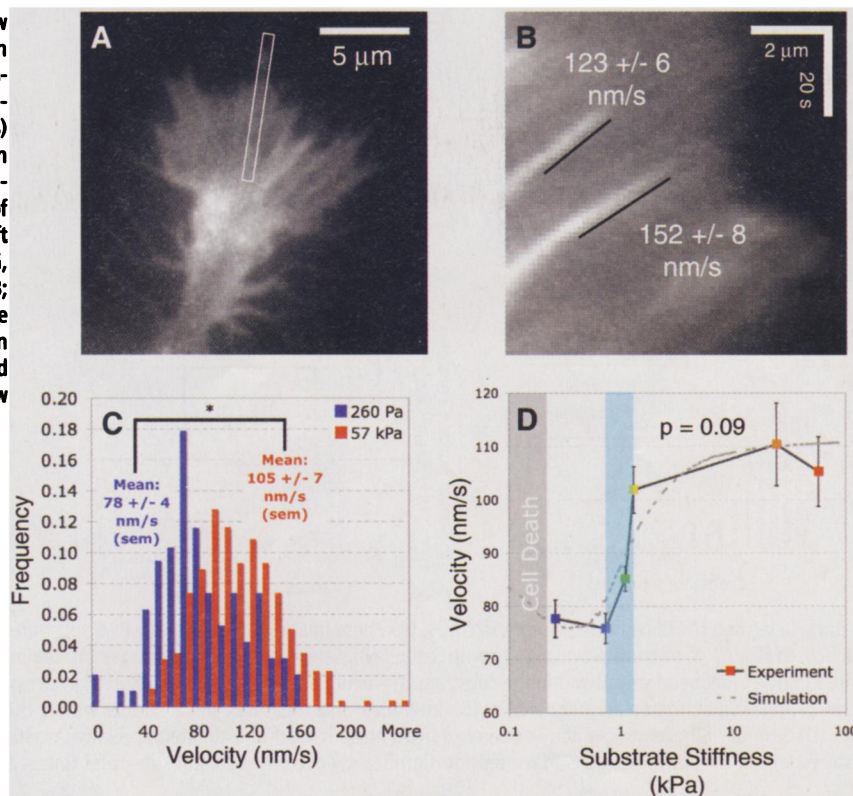


Fig. 3. Growth-cone filopodia F-actin retrograde flow rate abruptly transitions from low to high around an elastic modulus of $E = 1$ kPa. (A) EGFP-actin transfected ECFN growth cone. The rectangular box indicates a filopodium exhibiting retrograde flow. (B) Kymograph along region indicated in (A). GFP-actin features create diagonal streaks, allowing the measurement of F-actin retrograde flow. (C) Histogram of measured F-actin retrograde flow rates on stiff and soft substrates [stiff substrate (purple): $E = 260$ -Pa PAG, $n = 95$; soft substrate (red): $E = 57$ -kPa PAG, $n = 258$; $*P < 0.001$]. (D) Measurements of F-actin retrograde flow over a range of stiffness indicate a narrow region of sensitivity (light blue shaded region) and a trend statistically consistent with model predictions. Very low stiffness (gray region) results in poor cell viability.



provides considerable resistance to the motor force, substantially slowing retrograde flow. Eventually, the load becomes so great that the stochastic loss of one clutch leads to a cascading failure event, in which the unsupportable load shifts progressively to remaining bonds, further destabilizing the F-actin/clutch interaction. This quickly leads to an abrupt coupling failure where all clutches rapidly disengage, consequently unloading the substrate and causing it to snap back to its initial rest position. Thus, computational modeling of motor-clutch motility on soft substrates predicts the natural emergence of an oscillatory “load-and-fail” traction force dynamic characterized by protracted periods (~10 to 100 s) of increasing tension, followed by an abrupt coupling failure (Fig. 1, B and C).

In addition, simulations predict that these substrate stiffness-dependent changes in clutch dynamics lead to substantial differences in F-actin retrograde flow rates and the mean traction forces exerted on soft versus stiff substrates. On stiff substrates, short-lived F-actin/clutch interactions

create a “molecular friction” (16), where only a few clutches are engaged at any given time point. Lower average clutch numbers limit the total tension developed along engaged clutches, resulting in lower mean traction forces and higher rates of retrograde flow. On the other hand, load-and-fail dynamics on soft substrates result in higher numbers of engaged clutches on average, increasing the total tension developed along clutches, leading to slower retrograde flow velocity and greater transmission of traction forces (Fig. 1D and fig. S1). As the substrate becomes softer still, modeling predicts a slight increase in retrograde flow rate along with a slight decrease in traction forces (Fig. 1D). This occurs as the system spends a greater fraction of the time weakly loaded, resulting in longer times to generate sufficient tension to substantially resist the myosin motors (movie S1). Thus, a motor-clutch system is predicted to exhibit substrate stiffness-dependent changes in clutch dynamics that result in higher retrograde flow rates with lower traction forces on stiff substrates and lower retrograde

flow rates with higher traction forces on soft substrates.

To test these model predictions, we used green fluorescent protein (GFP)–actin transfected embryonic chick forebrain neurons (ECFNs) plated on soft (260 to 730 Pa) or stiff (1.3 to 57 kPa) polyacrylamide gel (PAG) substrates coated with polyethyleneimine as an adhesion promoter. Compliant PAGs embedded with 200-nm-diameter fluorescent fiducial marker beads allow the visualization of traction forces as deflections of beads from their rest position (17–19). Using dual-channel epifluorescence imaging in combination with a computational bead-tracking algorithm, we visualized F-actin dynamics in growth-cone filopodia and deflections of underlying marker beads to directly observe traction force transmission dynamics at 1- to 10-Hz frame rates (13).

With this system, we find that neurons exhibit a wide variety of region-specific traction force dynamics on compliant PAGs (fig. S2 and movie S2). Whereas axons, neurons, and growth cones exerted randomly directed and fluctuating tractions, growth-cone filopodia frequently displayed large, unidirectional bead deflections several times greater in magnitude than those from other regions of the neuron. Growth-cone motility was dependent on $\beta 1$ -integrin-mediated adhesion (fig. S3 and movie S3), consistent with our earlier studies that made use of magnetic bead force application (20).

When we examined the detailed time evolution of filopodial traction forces, we found that substrate-embedded marker beads deflected inwardly toward the growth cone and would occasionally snap back toward their rest position, indicative of the load-and-fail behavior predicted by the motor-clutch model when the substrate is soft (Fig. 2A, fig. S4, and movie S4). A time projection through movie S4 shows that filopodia exert unidirectional tractions along the filopodium axis (Fig. 2B). A kymograph along the axis of the filopodium shows that filopodium exert traction forces with load-and-fail dynamics similar to that predicted by the model, with cycle times on the order of tens of seconds (Fig. 2C). On occasions where more than one filopodium within a growth cone exerted observable tractions, we found substantial variation in both the amplitude and frequency of load-and-fail events (movie S4). This suggests that cells probably have stochastic fluctuations or spatial gradients in one or more motor-clutch parameters, leading to variable dynamics among individual filopodia. When filmed at 100-ms time intervals, we found that failure events occurred very abruptly, with detectable bead relaxations occurring in a single frame (Fig. 2D and fig. S6). Furthermore, loading often occurred immediately (<100 ms) after failure events, demonstrating that failures were attributable to transient clutch disengagement rather than filopodia retracting from the region entirely. We also found that increasing substrate stiffness resulted in an increase in the frequency

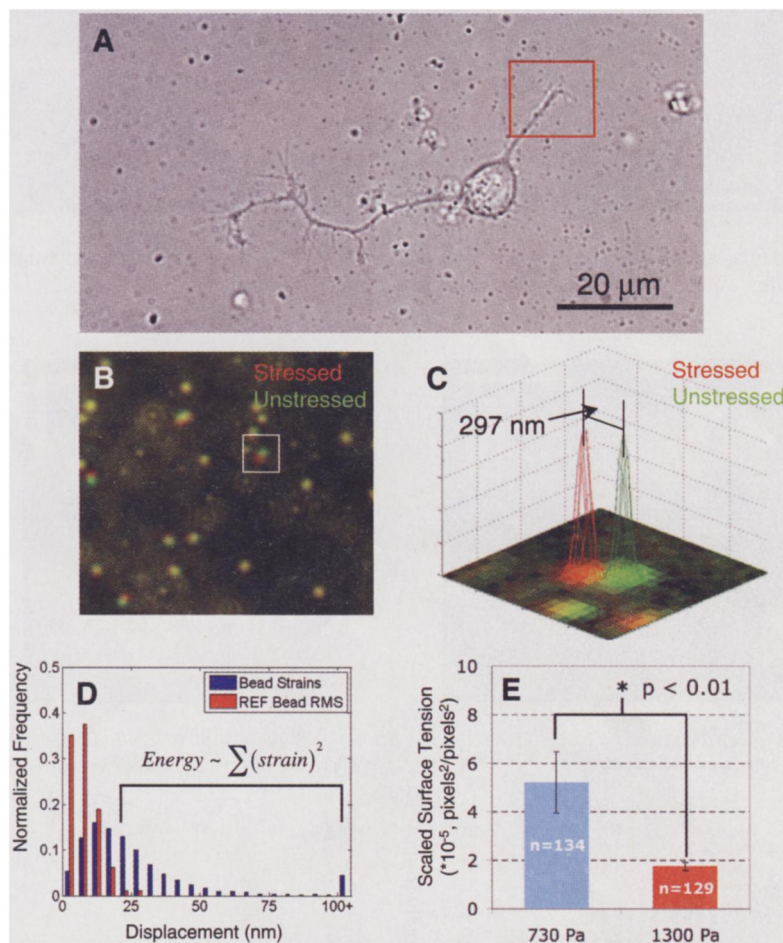


Fig. 4. Surface tension of ECFNs decreases on stiff PAGs. (A) Phase image of an ECFN on a PAG substrate. The red box indicates a traction-producing growth cone. (B) Stressed/unstressed images of region highlighted in (A) reveal bead strains within the substrate. The white box indicates a region of high stress. (C) Image processing of region highlighted in (B) identifies and measures bead strains within the substrate. (D) Sum of all bead strains above reference bead noise is used to estimate the relative elastic energy stored within the substrate. (E) Surface tension significantly decreases on stiff substrates (mean \pm SEM).

of failure events ($P < 0.03$) (fig. S5), which is consistent with the simulation. Together, these data reveal that filopodia exert traction forces with load-and-fail dynamics predicted by a stochastic model for the motor-clutch system on a soft substrate.

To test the model prediction that retrograde flow rate increases with increasing substrate stiffness, we tracked fluorescent GFP-actin features from growth cones of transfected ECFNs on PAG substrates imaged by means of epifluorescence (Fig. 3A). As growth cones crawl, polymerization at the leading edge stochastically gives rise to a fluctuating number of GFP-labeled actin filaments that constitute the filopodial F-actin bundle, creating alternately bright and dark F-actin features that can be quantitatively tracked via digital image analysis (13).

As with other motile cell types, the peripheral zone of growth cones exhibits rapid retrograde flow of polymerized actin (Fig. 3B and movie S5). Furthermore, the motion of GFP-actin features was myosin II-dependent (fig. S7) and never observed to move anterogradely (out of $n = 922$ features tracked), demonstrating that the major point of coupling failure lies between the F-actin/substrate interface, rather than between the myosin/F-actin interface. Creating kymographs along filopodia reveals motion of F-actin features that were tracked with a cross-correlation algorithm (13). Using this method, we found that retrograde flow was significantly slower on soft substrates ($P < 0.0001$) (Fig. 3C). Untransfected ECFNs also exhibited a similar response to substrate stiffness, suggesting that this effect is independent of GFP-actin (fig. S8). Filopodia on substrates from 730 to 1300 Pa showed high sensitivity to stiffness, abruptly increasing their retrograde flow rates as substrate stiffness increased (Fig. 3D, blue region). Once substrate stiffness exceeded a critical value of ~ 1300 Pa, retrograde flow rates became insensitive to stiffness, having a mean velocity of ~ 110 nm/s. On extremely soft substrates (≤ 84 Pa), ECFNs appeared unhealthy, often dying within 1 to 2 days (fig. S9). Thus, measuring the retrograde flow rate over a range of substrate stiffness revealed a trend not significantly different from that predicted by simulation ($P = 0.09$) and suggests that ECFN growth-cone filopodia may transition from load-and-fail dynamics to frictional slippage around 1 kPa (Fig. 3D).

Next, to test the model prediction of increased traction force transmission on softer substrates, we considered the amount of elastic strain energy exerted by ECFNs to displace individual marker beads from their rest position as the cell pulls on the elastic substrate (13). To estimate the elastic strain energy stored within the substrate, stressed images of marker beads during ECFN interaction were captured, followed by an unstressed image in which the cell was released from the substrate using trypsin (Fig. 4, A and B). Next, we measured the displacement of every marker bead in the field (Fig. 4C) and estimated the total stored

energy by summing the squared displacements of all marker beads above the noise and scaling the result according to the substrate stiffness (Fig. 4D). When normalized to the projected area of the cell, this metric can be considered as a “surface tension” between the cell and the substrate. Using this method, we find that ECFNs on soft PAGs have a threefold higher surface tension as compared with stiffer gels ($P < 0.01$) (Fig. 4E), in agreement with model predictions.

Together, these modeling and experimental results show that a motor-clutch retrograde flow mechanism naturally responds to substrate stiffness, with a very abrupt change around 1 kPa in the specific case of ECFNs grown in vitro. Substrate stiffness-dependent changes in clutch dynamics may serve as a basis for sensing environmental stiffness, providing differential inputs to mechanosensitive elements, ultimately transducing these signals into altered cell motility, cell morphology, and cell fate.

References and Notes

1. T. Yeung *et al.*, *Cell Motil. Cytoskeleton* **60**, 24 (2005).
2. C.-M. Lo, H.-B. Wang, M. Dembo, Y.-L. Wang, *Biophys. J.* **79**, 144 (2000).
3. L. A. Flanagan, Y. E. Ju, B. Marg, M. Osterfield, P. A. Janmey, *Neuroreport* **13**, 2411 (2002).
4. P. C. Georges, W. J. Miller, D. F. Meaney, E. S. Sawyer, P. A. Janmey, *Biophys. J.* **90**, 3012 (2006).
5. A. J. Engler, S. Sen, H. L. Sweeney, D. E. Discher, *Cell* **126**, 677 (2006).
6. T. Mitchison, M. Kirschner, *Neuron* **1**, 761 (1988).
7. K. Hu, L. Ji, K. T. Applegate, G. Danuser, C. M. Waterman-Storer, *Science* **315**, 111 (2007).
8. C. Jurado, J. R. Haserick, J. Lee, *Mol. Biol. Cell* **16**, 507 (2005).
9. L. B. Smilenov, A. Mikhailov, R. J. Pelham Jr., E. E. Marcantonio, G. G. Gundersen, *Science* **286**, 1172 (1999).
10. G. I. Bell, *Science* **200**, 618 (1978).
11. N. Q. Balaban *et al.*, *Nat. Cell Biol.* **3**, 466 (2001).
12. D. Riveline *et al.*, *J. Cell Biol.* **153**, 1175 (2001).
13. Materials and methods are available as supporting material on Science Online.
14. A. Mallavarapu, T. Mitchison, *J. Cell Biol.* **146**, 1097 (1999).
15. S. L. Gupton, C. M. Waterman-Storer, *Cell* **125**, 1361 (2006).
16. J. Howard, R. L. Clark, *Appl. Mech. Rev.* **55**, B39 (2002).
17. C. E. Kadow, P. C. Georges, P. A. Janmey, K. A. Benigno, in *Cell Mechanics, Methods in Cell Biology*, vol. 83, Y. Wang, D. E. Discher, Eds. (Academic Press, San Diego, CA, 2007), pp. 29–46.
18. R. J. Pelham, Y. Wang, *Proc. Natl. Acad. Sci. U.S.A.* **94**, 13661 (1997).
19. Y. L. Wang, R. J. Pelham, *Methods Enzymol.* **298**, 489 (1998).
20. J. N. Fass, D. J. Odde, *Biophys. J.* **85**, 623 (2003).
21. This research was supported by the Institute for Engineering in Medicine at the University of Minnesota, NSF (grant MCB-0615568), and the National Institute of General Medical Sciences (grant R01-GM-76177). We thank P. Letourneau, D. Bray, and E. Tuzel for stimulating discussions; N. Simha for helpful discussions on gel mechanics; N. Koyano for assistance with in ovo electroporation; and members of the Odde Lab, D. Seetapun, A. Bicek, M. Gardner, and T. Dahl for technical assistance.

Supporting Online Material

www.sciencemag.org/cgi/content/full/322/5908/1687/DC1

Materials and Methods

SOM Text

Figs. S1 to S12

Table S1

References

Movies S1 to S5

22 July 2008; accepted 29 October 2008

10.1126/science.1163595

Structure and Functional Role of Dynein's Microtubule-Binding Domain

Andrew P. Carter,^{1*} Joan E. Garbarino,^{2*} Elizabeth M. Wilson-Kubalek,³ Wesley E. Shipley,² Carol Cho,¹ Ronald A. Milligan,³ Ronald D. Vale,^{1†} I. R. Gibbons²

Dynein motors move various cargos along microtubules within the cytoplasm and power the beating of cilia and flagella. An unusual feature of dynein is that its microtubule-binding domain (MTBD) is separated from its ring-shaped AAA+ adenosine triphosphatase (ATPase) domain by a 15-nanometer coiled-coil stalk. We report the crystal structure of the mouse cytoplasmic dynein MTBD and a portion of the coiled coil, which supports a mechanism by which the ATPase domain and MTBD may communicate through a shift in the heptad registry of the coiled coil. Surprisingly, functional data suggest that the MTBD, and not the ATPase domain, is the main determinant of the direction of dynein motility.

Dyneins are AAA+ adenosine triphosphatases (ATPases) that power minus end-directed movement along microtubules (1). The cytoplasmic form of dynein serves many cellular functions including regulation of the mitotic checkpoint (2), organization of the Golgi apparatus (3), and the transport of vesicles, viruses, and mRNAs (4). Several human diseases, such as lissencephaly (4), primary ciliary dyskinesia (5), neural degeneration (6), and male infertility (7), result from dynein dysfunction.

The motor region of dynein (Fig. 1A) consists of a ring of AAA+ domains (four of which bind and hydrolyze ATP), a mechanical element (termed the “linker”) that is likely involved in driving motility (8, 9), and a ~ 15 -nm “stalk” that has a microtubule-binding domain (MTBD) at its tip. The stalk, which emerges from AAA4 (the fourth nucleotide-binding AAA+ domain in the ring), extends as one α helix of an antiparallel coiled coil (termed CC1), forms the small, globular MTBD, and then returns as the partner helix